Adaptive Optics Simulations for the European Extremely Large Telescope

Richard M. Clare, Miska Le Louarn, Sylvain Oberti, and A. Garcia-Rissman

European Southern Observatory,

Karl-Schwarzschild-Straße 2, Garching bei München, 85748, Germany.

ABSTRACT

Simulations of adaptive optics (AO) for the European extremely large telescope (EELT) are presented. For Shack-Hartmann wavefront sensors for the laser guide star (LGS) based systems, the simulations show that without the Rayleigh fratricide effect, central projection of the laser is preferable to side projection, the correlation or matched filter centroiding algorithms offer superior performance to a traditional center-of-gravity approach, the optimum sampling of the detector is approximately 1.5 pixels per FWHM of the non-elongated spot, and that at least 10×10 pixels are required. The required number of photo-detection events from the LGS per frame per subaperture is of the order of 1000. Correction of segmentation errors with a Shack-Hartmann wavefront sensor (WFS) has also been investigated; atmospheric turbulence dominates these segmentation errors. The pyramid WFS is also simulated for the EELT, showing that modulation of the pyramid will be necessary.

Keywords: adaptive optics, wavefront sensing, laser guide stars.

1. INTRODUCTION

At the current point in time, a number of extremely large telescopes (ELTs) of primary mirror diameters 20-42 m are in the design stages, such as the thirty meter telescope (TMT),[1] the giant Magellan telescope (GMT),[2] and the European Southern Observatory's 42m diameter European ELT (EELT).[3] Adaptive optics (AO) will be required to overcome the degradatory effects of the atmosphere in order to successfully utilize the unprecedented resolution of these ELTs.

The EELT will require a number of different AO systems, each designed to meet its instruments' particular science requirements. Single conjugate AO (SCAO) will use a natural guide star (NGS) to provide correction over a small field of view (FOV) with a single deformable mirror (DM). Due to the sky coverage constraints of NGS systems, multiple laser guide star (LGS) based systems are also required for the EELT. Ground layer AO (GLAO) will provide a modest correction over a large FOV, with a ground conjugated DM. Laser tomography AO (LTAO) will provide improved correction compared to GLAO, but over a much smaller field, again with a single DM. The multi conjugate AO (MCAO) system is similar to LTAO, except the correction will be applied with multiple DMs conjugated to different layers. For a more detailed description of these AO systems, see Ref. 4.

In Section 2, we outline the methodology of the simulations of the LGS wavefront sensor (WFS) for the LGS AO systems of the EELT. Then in Section 3, we present the results of the LGS simulations. In Section 4, we investigate the ability of the SCAO system to correct the deformations of the segmented primary of the EELT due to wind. In Section 5, we consider the use of a pyramid WFS for the EELT. Conclusions for this work are drawn in Section 6.

Further author information: Send correspondence to R.M.C.

Ph: +49 89 3200 6504,

Email: rclare@eso.org

2. LGS SIMULATION THEORY

The LGS WFS(s) for the EELT will be Shack-Hartmann. For a Shack-Hartmann WFS with a LGS at a finite height and non-zero thickness of the sodium layer, the spot at each subaperture is elongated due to the parallax effect. The elongation of the Shack-Hartmann spots, η, for the LGS WFS is approximately given by[5]

$$\eta = \frac{\cos(\zeta)bt}{h^2}, \tag{1}$$

where ζ is the zenith angle, b is the baseline distance between the launch telescope and the subaperture, t is the thickness of the sodium layer, and h is the mean height of the sodium layer above the telescope. This elongation of the LGS Shack-Hartmann WFS images will cause significant degradation in the centroid measurement error in each subaperture, and consequently in the reconstructed wavefront and hence Strehl. In this section, we describe the methodology for calculating the wavefront measurement error, σ, for a given set of design and environmental parameters. The purpose of these simulations is to determine the optimal laser launch position, centroiding algorithm, detector sampling and FOV, and the required laser power.

2.1. LGS WFS image generation

Firstly, we generate the elongated LGS WFS images. The mean (unshifted) LGS WFS images, $I(x, y)$, are generated using the code developed at the W.M. Keck Observatory and described in Ref. 6. This code assumes geometric optics projection on the uplink and downlink paths. The intensity at each pixel is a numerical integral of the intersection of the laser beam with the sodium profile over the pixel FOV. The code has been verified against Eq. (1) by fitting the full width at half maximum (FWHM) of the LGS WFS images for a Gaussian sodium profile, gaining very good agreement.

The shifted LGS images WFS images, $\tilde{I}(x, y)$, are created by jittering the mean images by (x_0, y_0) with the Fourier shift theorem

$$\tilde{I}(x, y) = \mathcal{F}^{-1}\big(\mathcal{F}\big(I(x, y)\big) \exp[j2\pi(x_0 u + y_0 v)]\big), \tag{2}$$

where $\mathcal{F}$ and $\mathcal{F}^{-1}$ are the Fourier and inverse Fourier transforms, and (u, v) are the coordinates in Fourier space. The jitter is assumed to be Gaussian distributed with variance σ_j^2.

The noisy LGS images, $I'(x, y)$, are then created by adding photon noise as a Poisson process for each pixel to the jittered image, $\tilde{I}(x, y)$, and adding Gaussian distributed read noise with a standard deviation of σ_r electrons per pixel per readout. This set of assumptions creates negative values for some pixels in $I'(x, y)$. These negative pixels are clipped to zero, unlike in the Thomas paper.[7]

2.2. Centroiding Algorithms

In this paper, we consider five algorithms for calcualting the estimate of the jitter, $(\hat{x}_0, \hat{y}_0)$ of the elongated LGS WFS spots: center-of-gravity (COG), COG with thresholding (THRESH), weighted COG (WCOG), correlation (CORR), and matched filter (MF). We describe each of these algorithms in turn here.

(1) The COG algorithm for estimating the tip/tilt in each subaperture is defined by[7]

$$\hat{x}_0 = \frac{\Sigma x I'(x, y)}{\Sigma I'(x, y)}, \qquad\qquad \hat{y}_0 = \frac{\Sigma y I'(x, y)}{\Sigma I'(x, y)}. \tag{3}$$

A special case of the COG algorithm is the quad-cell (QC), where because the LGS images are poorly sampled by the 2×2 pixels, the relationship between the centroid, $\hat{x}_0$, and the pixel intensities, $I'(x, y)$, is given by

$$\hat{x}_0 = g\frac{I'_{11} + I'_{12} - I'_{21} - I'_{22}}{\Sigma I'(x, y)} \tag{4}$$

where the QC gains, g, are

$$g = \sqrt{\frac{\pi}{2}}\theta, \tag{5}$$

and θ is the rms spot size in the direction of centroiding. In this paper the QC gains are calculated in x and y from the elongation and orientation of each spot as per Ref. 8.

(2) THRESH is a variation of COG, where the threshold, T, is subtracted from the image, and the negative pixels are then zeroed,

$$I_t(x,y) = \begin{cases} I'(x,y) - T & I'(x,y) - T > 0 \\ 0 & \text{otherwise.} \end{cases} \tag{6}$$

The thresholded image, $I_t(x,y)$, is then centroided using Eq. (3). In the simulations, the threshold is optimized for each parameter set and subaperture.

(3) The WCOG algorithm for finding the tilt estimate is given by[7]

$$\hat{x}_0 = g\frac{\Sigma x W(x,y)I'(x,y)}{\Sigma I'(x,y)}, \qquad\qquad \hat{y}_0 = g\frac{\Sigma y W(x,y)I'(x,y)}{\Sigma I'(x,y)}, \tag{7}$$

where $W(x,y)$ is the weighting function, and g, the gain, is

$$g = \frac{N_{Samp}^2 + N_W^2}{N_W^2}, \tag{8}$$

where N_{samp} and N_W are the number of pixels per FWHM of the image and weighting function respectively. Thomas identifies using either the mean image or Gaussians as the weighting function. We find that using a Gaussian weighting works better than using the mean image for non-Gaussian sodium profiles. N_W is optimized at each photon level and for each subaperture. At lower photon counts it is best to have a smaller N_W, and larger N_W at higher photon counts.

(4) The CORR algorithm that we employ in this paper is defined by Poyneer in Ref. 9. The cross-correlation, $C(x,y)$, of the noisy image and the mean image is given by

$$C(x,y) = \mathcal{F}^{-1}\left\{ \left[\mathcal{F}\{I(x,y)\}\right]^* \mathcal{F}\{I'(x,y)\} \right\}. \tag{9}$$

The estimate of the jitter is then given by the position of the maximum of $C(x,y)$. Poyneer offers three methods for finding the maximum of $C(x,y)$: fitting a parabola, fitting a Gaussian, and using the THRESH algorithm on C(x,y). We found that for noisy elongated LGS spots the last method yields the best performance. For CORR, the Fourier transform product of Eq. (9) can be zeropadded to increase the resolution of $C(x,y)$. Initial simulations showed that an oversampling factor of 4 was sufficient, there was little improvement in the error variance in oversampling by more than this, whilst the simulations are slowed down significantly the larger the oversampling.

(5) The MF, or noise-weighted least squares, algorithm is defined in Ref 10. The estimate of the jitter on the LGS WFS image, $(\hat{x}_0, \hat{y}_0)$, from the noisy LGS image $I'(x,y)$ is

$$(\hat{x}_0, \hat{y}_0) = (Q^T N^{-1} Q)^{-1} Q^T N^{-1} (I'(x,y)/N_p - I(x,y)), \tag{10}$$

where $I(x,y)$ is the normalized mean image, N, the noise covariance, is the sum of the shot noise contribution and read noise, σ_r,

$$N(x,y) = N_p I(x,y) + \sigma_r{}^2. \tag{11}$$

Q is the interaction matrix for the matched filter approach, and is defined by

$$Q = \begin{pmatrix} Q_x & Q_y \end{pmatrix} = \begin{pmatrix} \frac{\partial I(x,y)}{\partial x_0} & \frac{\partial I(x,y)}{\partial y_0} \end{pmatrix}. \tag{12}$$

The partial derivatives of $I(x,y)$ with respect to x_0 and y_0 can be found by expressing the shifted LGS image $I'(x,y)$ by

$$I'(x,y;x_0,y_0) = N_p \mathcal{F}^{-1}\left\{ \mathcal{F}\{I(x,y)\} \exp(-j2\pi(ux_0 + vy_0)) \right\}, \tag{13}$$

The partial derivatives of the NGS images in the x and y directions evaluated at $(x_0, y_0)=(0,0)$ are

$$\frac{\partial I}{\partial x_0}\bigg|_{(x_0,y_0)=(0,0)} = N_p \mathcal{F}^{-1}\left\{-j2\pi u \mathcal{F}\{I(x,y)\}\right\}, \qquad \frac{\partial I}{\partial y_0}\bigg|_{(x_0,y_0)=(0,0)} = N_p \mathcal{F}^{-1}\left\{-j2\pi v \mathcal{F}\{I(x,y)\}\right\}. \quad (14)$$

The derivatives of the reference image, $I(x,y)$, with respect to the jitter in x and y are calculated with the use of the Fourier transform (FT). It should be noted that the real-time computation for the MF does not require a FT operation, unlike the correlation method.

2.3. Subaperture error calculation

We calculate the measurement error variances in the x and y directions, σ_x^2 and σ_y^2 respectively, for a given subaperture in the same manner as Thomas[7, 11]

$$\sigma_x^2 = \left(\frac{2\pi}{N_{samp}}\right)^2 \left\langle (\hat{x}_0 - x_0)^2 \right\rangle, \qquad \sigma_y^2 = \left(\frac{2\pi}{N_{samp}}\right)^2 \left\langle (\hat{y}_0 - y_0)^2 \right\rangle, \quad (15)$$

where $\langle . \rangle$ indicates an ensemble average.

The noise covariance matrix, C_N, is a block diagonal matrix of the form

$$C_N = \begin{bmatrix} \sigma_{x,1}^2 & \sigma_{xy,1}^2 & 0 & 0 & 0 \\ \sigma_{xy,1}^2 & \sigma_{y,1}^2 & \ddots & 0 & 0 \\ 0 & \ddots & \ddots & \ddots & 0 \\ 0 & 0 & \ddots & \sigma_{x,N}^2 & \sigma_{xy,N}^2 \\ 0 & 0 & 0 & \sigma_{xy,N}^2 & \sigma_{y,N}^2 \end{bmatrix}. \quad (16)$$

where $\sigma_{x,n}^2$ is the subaperture error variance in the x direction for the nth subaperture, $\sigma_{y,n}^2$ is the subaperture error variance in the y direction for the nth subaperture, and $\sigma_{xy,n}^2$ is the subaperture error covariance between x and y for the nth subaperture.

2.4. Wavefront error calculation

We calculate the wavefront error due to measurement noise, σ^2 (rads^2), from the noise covariance matrix with[12]

$$\sigma^2 = \frac{1}{N_{act}} TR\{A C_N A^T\}, \quad (17)$$

where A is the command matrix, TR is the trace operator, and N_{act}, the number of actuators, is a normalization factor. The command matrix A is a least squares reconstructor and was calculated in an end-to-end simulation for a SCAO case ($\lambda=0.7\mu$). The command matrix is of dimension $N_{act} \times 2N_{sa}$.

3. LGS SIMULATION RESULTS

In this section, we detail the assumptions and parameters used for the simulations, and present simulation results for the LGS AO systems. The simulations are run in parallelized matlab code over a cluster. In order to speed up the simulations, only 1/8th of the subapertures are simulated, and the remainder of the covariances in C_N are filled in from symmetry. The centroiding algorithms were verified for a single subaperture and Gaussian spot against the analytical and simulation results of Thomas.[7, 11]

3.1. Simulation Parameters

The parameters and their nominal baseline values for the simulations are shown in Table 1. The baseline detector design is 20×20 pixels with $\sigma_r=3e^-$. Unless otherwise stated, these are the values used. The chosen value of the residual jitter, σ_j, is 0.0656 arcsec, which is the mean SCAO residual centroid to achieve a Strehl of 0.7 in K band.

Table 1. System and atmospheric parameters for Section 3.

Parameter	Symbol	Value
Telescope diameter	D	42 m
Number of subapertures	N_{sa}	84×84
Number of actuators	N_{act}	5402
Zenith angle	γ	0
Mean height of sodium above telescope	h	86km
Read noise/pixel/readout	σ_r	$3e^-$
Number of pixels	N_{pix}	20×20
Trials per subaperture	-	500
Residual rms jitter	σ_j	0.0656 arcsec
Image FWHM	θ	1.4 arcsec
Laser launch position	-	(0,0)
Number of photons/subaperture/readout	N_p	1000
Number of pixels/FWHM	N_{samp}	2
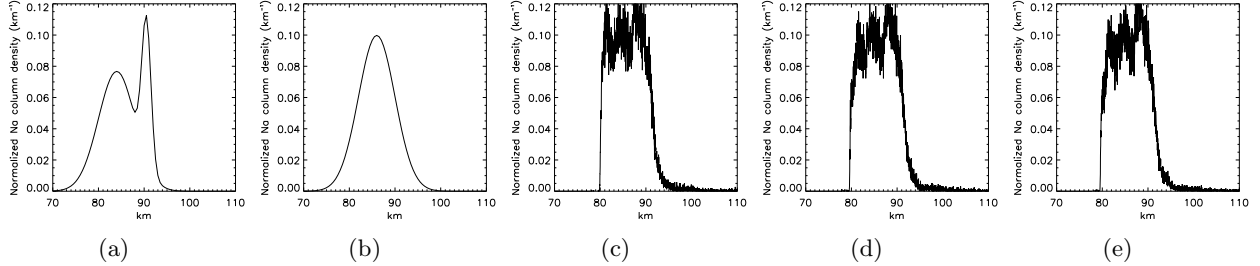
Figure 1. The normalized sodium profiles: (a) double Gaussian, (b) single Gaussian, (c) LIDAR frame 4, (d) LIDAR frame 5, and (e) LIDAR frame 6.

3.2. Sodium Profiles

Two fitted sodium profiles are chosen as the baseline in this paper. The first is the sum of two Gaussians, one of σ=3.5km located at h=84.0 km above the telescope and the other σ=1km located at h=94.5 km above the telescope as shown in Fig. 1(a). This profile is referred to as the double Gaussian. The maximum FWHM for the double Gaussian profile for the EELT at zenith is 7.3 arcsec. The second fitted profile used in this paper is shown in Fig. 1(b), and is a Gaussian of σ=4km centred at h=86km above the telescope, and is referred to as the single Gaussian. The maximum FWHM for the single Gaussian profile is 5.7 arcsec. These two sodium profiles were chosen as best-fits to acquisition camera images at the W.M. Keck Observatory.[5]

When investigating the LGS aberrations, which arise due to the temporal evolution of the sodium layer, we use a set of LIDAR profiles taken with the University of Western Ontario LIDAR.[13] This set of profiles has a temporal resolution of 72 seconds, and a spatial resolution of 24m. Three consecutive LIDAR profiles are shown in Fig. 1.

3.3. Parameter Characterization

The wavefront error for the five candidate algorithms is plotted vs the number of detected photons, N_p, in Fig. 2(a) for the baseline parameters in Table 1 and the double Gaussian sodium profile. There is a clear hierarchy in performance, with COG the worst at all signal levels, followed by THRESH and then WCOG. The two best algorithms are those that explicitly use knowledge of the structure of the sodium layer (CORR and MF). The dotted line indicates the wavefront error due to the input jitter alone (23 nm). So, of the five algorithms, only the MF with 900 photons can realise the closed loop jitter requirement to achieve a Strehl of 0.7 in K band.

Fig. 2(b) shows the wavefront error for LIDAR profile 1, the single and double Gaussian sodium profiles for both the COG and MF algorithms for the parameters in Table 1. For the COG algorithm, there is no significant
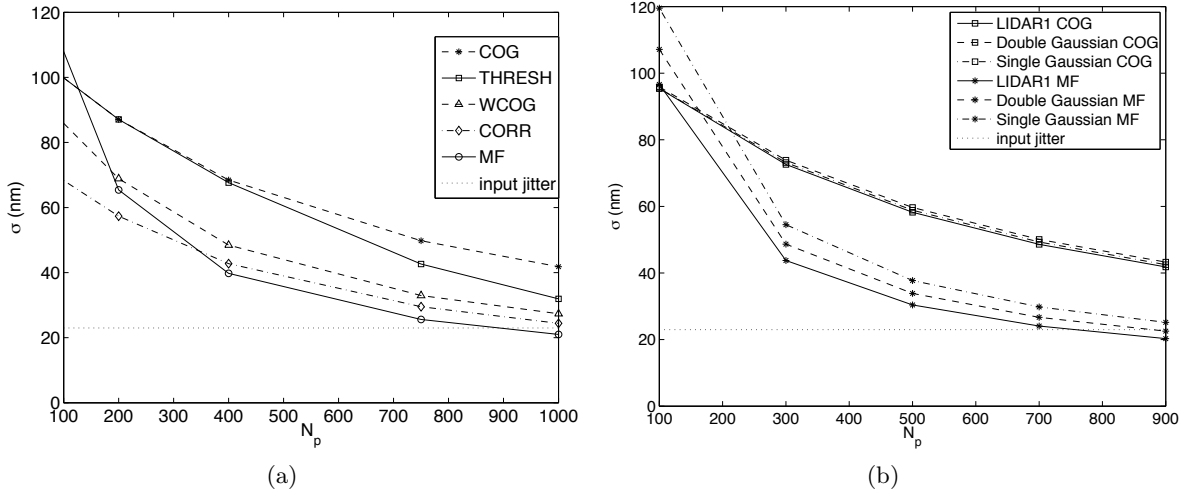
Figure 2. The wavefront error versus number of photons per subaperture for (a) different algorithms, and (b) different sodium profiles. The dotted curve is the wavefront error corresponding to the input jitter.

Table 2. The multi-dimensional optimization of N_{pix}, pixel scale, and algorithm for the single Gaussian profile and θ=1.4 arcsec.

N_p	N_{pix}	Pixel scale (arcsec/pix)	Algorithm	σ (nm)
100	-	-	-	-
300	4×4	1.05	CORR	21.1
500	6×6	1.05	CORR	19.2
700	6×6	1.05	CORR	17.6
900	6×6	1.4	CORR	16.2

difference in performance between the three sodium profiles. This is not surprising as all three profiles have similar FWHMs. For the MF algorithm, however, the performance is better for the sodium profiles that have more structure; the LIDAR profile, followed by the double Gaussian and then the single Gaussian. It takes 700 photons to achieve the wavefront error corresponding to the input jitter for the LIDAR profile and 900 photons for the single Gaussian profile.

3.4. Multi-dimensional Optimization

We optimize the number of pixels, plate scale and WFS algorithm simultaneously for a given paramater set. The optimum pixel values, plate scales and algorithms for the range of 100-900 photons are tabulated in Table 2 for θ=1.4 arcsec and σ_r=3e$^-$. The range of N_{pix} is 2-20 with pixel scales of [0.35 0.7 1.05 1.4 2.1 4 8] arcsec and all 5 algorithms are considered. If the minimum wavefront error for any combination of pixels, pixel scale and algorithm at any photon level exceeds the wavefront error corresponding to the input jitter (23nm), then the row in the table is left blank (-). In these cases, the optimization can choose non-sensical combinations that merely return a centroid close to zero, such as 2x2 correlation. This is an artefact of the fact that we are simulating a closed loop system with small residual jitters.

Table 2 shows the optimum algorithm is CORR, the plate scale is $1.5\times\theta/2$, and the optimum N_{pix} is 6×6. Similar results in terms of pixel scale, number of pixels and algorithm (either the CORR or MF) were obtained for other sodium profiles. However, this result is obtained assuming known reference centroids and that the sodium layer does not evolve. In the next subsection, we also consider the quasi-static LGS aberrations.

3.5. Laser Guide Star Aberrations

So far we have considered the measurement error that arises in centroiding about a known reference centroid. However, the reference centroids will not be known perfectly as they will change as the sodium layer evolves,
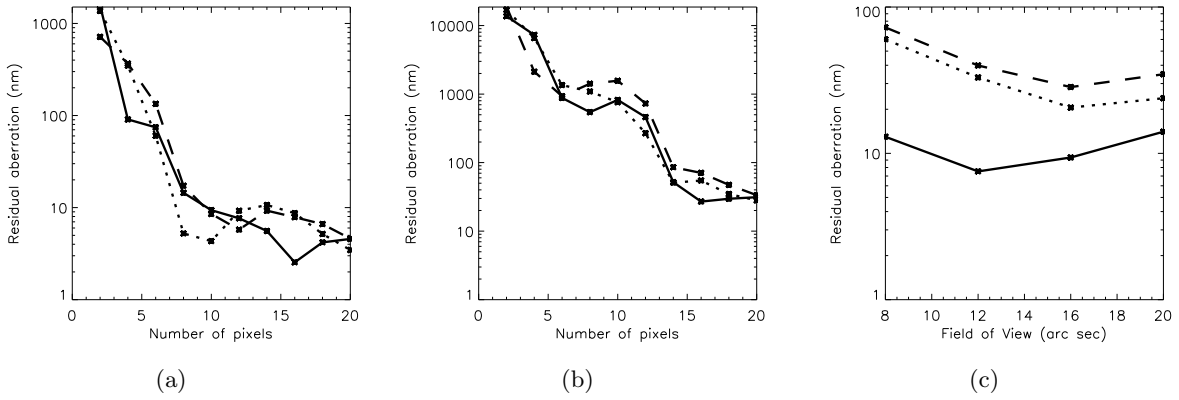
Figure 3. The residual LGS aberrations (nm) between LIDAR frames 5 and 4 (solid line), 6 and 5 (dashed line) and 6 and 4 (dotted line) for: (a) central projection versus number of pixels for 1 arcsec pixels, (b) side projection versus number of pixels for 1 arcsec pixels, (c) central projection QC versus FOV.

or the seeing changes.[5, 6] In practice, the reference centroids will be estimated with a low bandwidth WFS (LBWFS) using a fraction of the light from the NGS. However, residual aberrations will still be seen due to the lag in measuring and updating reference centroids. The FOV of the detector strongly influences the magnitude of the LGS aberrations, as the LGS aberrations are a function of the biases introduced by truncating the LGS WFS spots.

Since the LGS aberrations are a function of the detector properties, we also need to simulate them in optimizing the detector. In order to estimate the LGS aberrations we use the code described in Ref. 6. For the side-projected Keck II LGS AO system, the measured aberrations are dominated by astigmatism and coma. However, for a centrally projected LGS system, the LGS aberrations are largely radially symmetric modes: spherical aberration, 5th order spherical and so on. This has been verified experimentally by Lardiere.[14]

In order to estimate the LGS aberrations for the EELT with respect to the FOV (number of pixels) of the detector we estimate the quasi-static aberrations for a series of LIDAR profiles. Because the LGS aberrations can largely be corrected by updating the reference centroids for the LGS WFS, we consider the difference in aberrations between consecutive LIDAR frames (those shown in Fig. 1). This difference then represents the residual LGS aberrations assuming that the LGS aberrations are perfectly corrected when the reference centroids are updated. The set of LIDAR profiles has a temporal resolution of 72 seconds.

Fig. 3 shows the LGS aberrations for central projection of the laser and side projection of the laser versus number of pixels (each 1.0 arcsec, the optimum from Table 2), and for quad-cells versus FOV. For central projection, the LGS aberrations are unacceptably high if there are fewer than 8×8 pixels with this sampling. With 8x8 pixels or more, the LGS aberrations are relatively flat, and are at more acceptable levels of 5-10 nm. For side projection, at least 14×14 pixels are required due to the extra elongation. Also, the aberrations are not confined to the radially symmetric modes either, with significant coma and astigmatism. It is significant that the residual LGS aberrations are significantly larger for the QC than multiple pixels, for the same FOV. For the QC, the LGS aberrations are of the order 10-30 nm for a 20 arc sec FOV, whereas they are of the order 5-10 nm for 20x20 1.0 arc sec pixels for the same sodium profiles. The reason for this difference is because the QC centroid is not the same as the centre-of-mass of the centroid, thus introducing a bias in the centroid measurement.[5]

3.6. Total LGS Errors

The total LGS error considered here is the sum of the LGS aberrations and the centroiding wavefront error, σ. We plot the total LGS error in Fig. 4 versus the number of pixels for central and side projection of the laser. This is for the optimum case of CORR and 1.05 arcsec/pixel for the single Gaussian, and the LGS aberrations are averaged over the three LIDAR profiles From Fig. 4 we see that 10×10 pixels is sufficient for central projection and 16×16 pixels sufficient for side projection for this sodium profile and LIDAR set. Fig. 4 shows that central
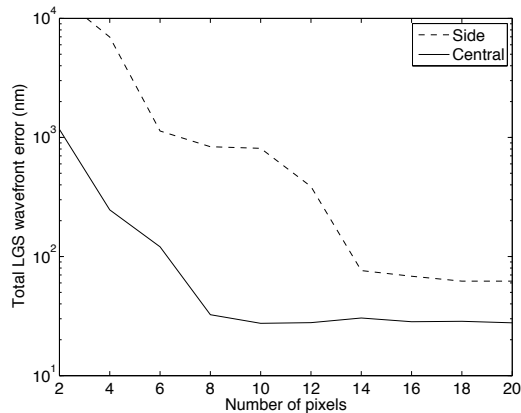
Figure 4. The total LGS error versus number of pixels for central (solid line) and side (dashed line) projection of the laser for single Gaussian profile, CORR and 1.05 arcsec pixels.

projection of the laser is clearly preferable to side projection from a WFS perspective and ignoring the effect of Rayleigh fratricide.

It is of interest to compare the optimum of 10×10 pixels of dimension 1.05 arcsec for central projection with other existing and planned systems (i.e. a FOV of 10.5x10.5 arcsec). The Keck II LGS AO system has QCs with a total FOV of 6.0 arcsec x 6.0 arcsec.[6,8] The elongation with the EELT centrally projected is 2.1 times the side elongation of Keck. Scaling the Keck system to ELT proportions gives a FOV of 12.6×12.6 arcsec. The TMT plan to employ the radial format CCD with 16x4 pixels in the outer ring of subapertures of dimension 0.5 arcsec.[10] This gives a FOV for the outer ring of subapertures of 8.0 × 2.0 arcsec. Scaling this to the EELT (42m vs 30m) would give a FOV of the outer ring of 11.2x2.8 arcsec. The scaling of Keck and TMT detectors to EELT size yield FOVs of approximate agreement with those calculated in this paper for the EELT.

3.7. Photon Requirements

Laser power is an important design cosideration for the EELT AO systems, and in this subsection we use our simulation tool to consider the required number of photo-detection events per subaperture for the MCAO/LTAO modules to achieve the same residual jitter as a SCAO Strehl of 0.7 in K band. The required photons for GLAO is expected to be significantly lower due to the lesser correction.

The required number of photo-detection events is determined as the point where the wavefront error is equal to the wavefront error due to the residual jitter alone. This definition specifies the number of photons needed to close the loop with the required residual jitter, and hence Strehl.

In order to estimate the required number of photons for the LGS WFS, we simulate the baseline detector (20x20 pixels, 0.8 arcsec/pixel (1.5 pixels per FWHM on a spot size of 1.1 arcsec), σ_r=3e$^-$), central projection of the laser, and the MF algorithm. Two of the most important environmental parameters are the sodium FWHM, t (here we assume a Gaussian FWHM only) and the non-elongated spot size (FWHM) on the detector, θ. We plot the required number of photo-detection events versus these two key parameters in Fig. 5, and make a linear best fit function of the required photo-detection events versus these two parameters. The linear best fits of the required detected photons versus t and θ, are respectively

$$N_p(t) = 141.4t - 468 \qquad 5 \text{ km} < t < 10 \text{ km} \tag{18}$$
$$N_p(\theta) = 290\theta + 630 \qquad 0.9 \text{ arcsec} < \theta < 1.8 \text{ arcsec.} \tag{19}$$

From Fig. 5, it can be seen that in median conditions (10km Na FWHM, 1.1 spot FWHM) of the order of 900 photons are required. However, in significantly worse conditions, in terms of either spot FWHM or sodium FWHM, the detected photon requirement can be in excess of 1000 photons.
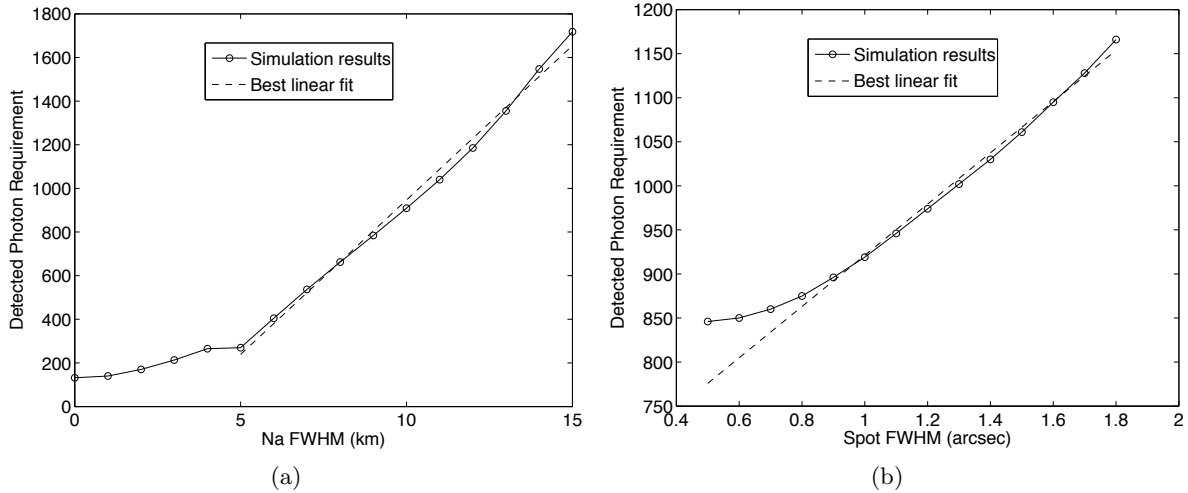
Figure 5. The required detected photons to achieve the equivalent wavefront error of a residual jitter of 0.0656 arcsec versus (a) the sodium FWHM for a Gaussian sodium profile, and (b) the FWHM of the LGS spot in the non-elongated direction on the detector. For both curves, linear best fits are superimposed over the linear regions.

With side projection of the laser under the same assumptions, 1560 photons are required to achieve the wavefront error equivalent to the input jitter, compared to 910 for central projection, an increase in laser power of 1.7.

4. CORRECTION OF THE SEGMENTATION RESIDUALS BY A SCAO SYSTEM

In this section, we investigate the ability of a SCAO system, tuned to correct atmospheric turbulence, to correct for the shape of the segmented primary mirror of the EELT. Indeed, the effect of wind on the primary mirror (M1) produces deformations of its shape, which will not be all corrected by the active system. Therefore, a residual will be seen by the AO system. The baseline 84x84 SCAO system is used to see how these residuals are correctable. Previous studies have extensively studied the ability of AO systems to correct for co-phasing error (see for example Ref. 15). However here we are specifically interested in a system tuned for turbulence (i.e. for example without spatial filter, and with a sampling adapted for turbulence).

4.1. Modal analysis

The telescope simulation provides a modal decomposition of the eigenmodes of the M1 control system. The highest spatial frequencies are best sensed, because edge sensors provide a very localized measurement. The lowest spatial frequencies are badly sensed. Some primary mirror modes are shown in Fig. 6(a). The modes with the lowest rank are those containing the most high frequencies (i.e. segment to segment aberrations). Of course, the opposite is true for an AO system. It measures and corrects very well low spatial frequencies.

To quantify this, we have fed each primary mirror aberration into the AO system model. The AO loop sees only this aberration, and tries to correct it. We let the AO loop converge for 20 iterations on a given static primary mirror mode and compare the input and output wavefront errors to deduce the efficiency of the AO correction. This is repeated for each mode of the primary. The results can be seen in Fig. 6(b). We can see the confirmation that low spatial order modes are much better corrected than the high spatial order ones. Note that each M1 mode was scaled to produce a measurable signal on the WFS and are not therefore representative of the amount of turbulence seen in reality on M1.

One has to notice that here the AO system is not working in a regime for which it was designed for. Indeed, for the lowest spatial frequencies, the spots of the Shack-Hartmann sensor are diffraction limited, whereas in a functionning regime (with turbulence), those spots will be seeing limited. This produces a gain effect. This gain is however taken into account by letting the AO loop converge before measuring the residual phase error.
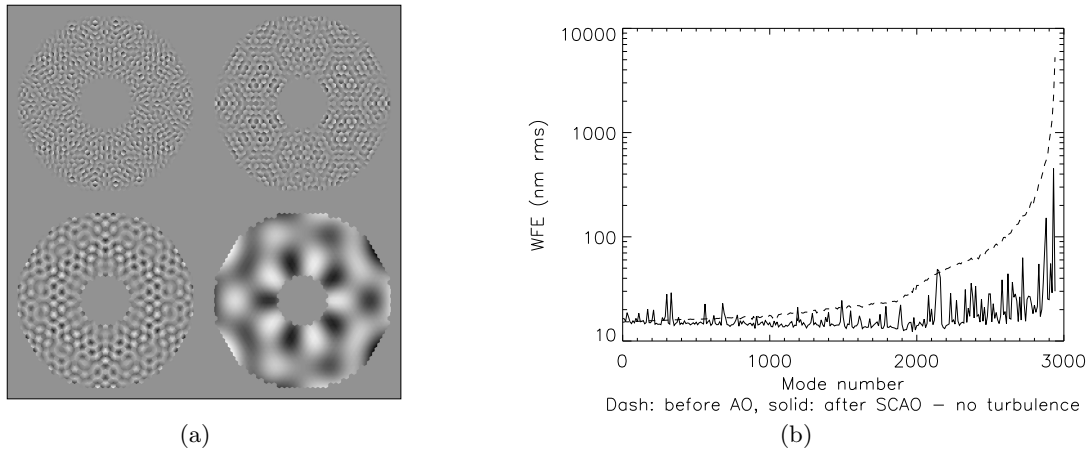
(a)   (b)

Figure 6. Performance of the AO system to correct M1 aberrations: (a) pictures of the M1 modes (from top left to bottom right), M1 modes 500, 1000, 2000 and 2900, and (b) the normalized wavefront errors before (solid) and after (dash) correction by AO.
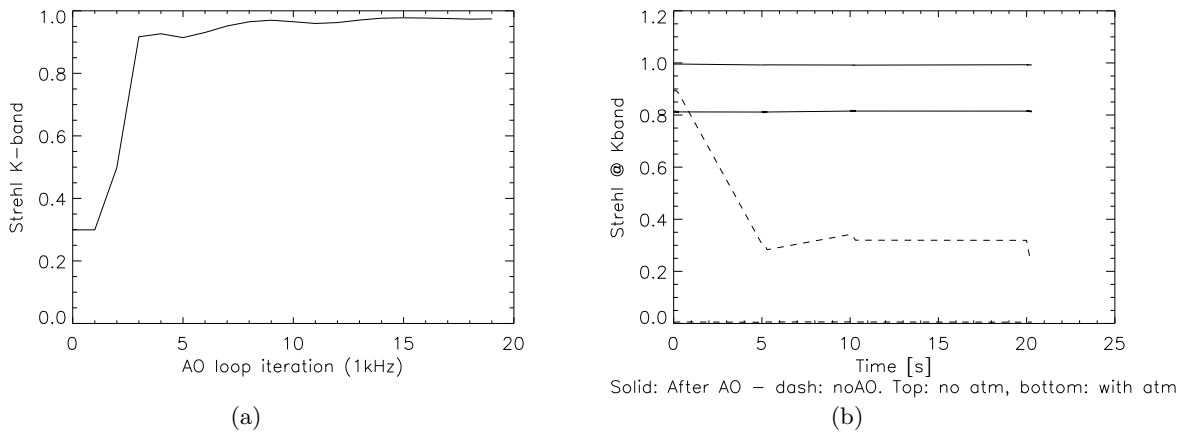

(a)   (b)

Figure 7. Performance of the AO system to correct M1 aberrations

The same experiment was repeated using an extended object in the SH sensor (to make a bigger spot), but no significant differences were seen in the results.

4.2. Case study

In the previous section, the segmentation errors were investigated mode by mode, with unrealistic amplitudes for some modes. Here, we analyze a typical realization of a primary mirror aberration. In this case, the primary mirror is subjected to wind, and its shape is left to evolve. After a few seconds, the shape of the primary is presented to the AO system. The results can be seen on Fig. 7(a). In this extreme case, the Strehl before AO is only 30% in the K-band. However, most of the aberrations are low (spatial) order and they are very well corrected by the AO system, as can be seen (over 95% of Strehl after a few iterrations).

If turbulence is added on top of the segmentation errors, we can confirm that the AO system is robust to both types of wavefront errors present simultaneously. This is demonstrated in Fig. 7(b). The solid lines show the results after the AO correction. Dashed lines before AO. The top line in each family is without the atmosphere (but with segmentation error), and the bottom line when both error sources are present. To investigate the temporal evolution of the main mirror aberrations, several points in time in the time series of mirror shapes were taken. However, each time step was considered to be static for the AO system. We notice that at the start,
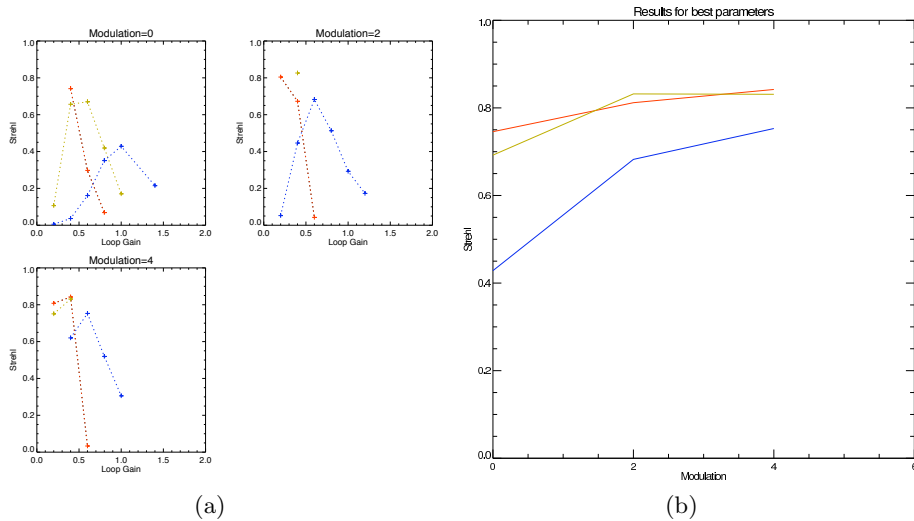
Figure 8. Performance of the pyramid WFS on the EELT: (a) as a function of loop gain for different modulations, and (b) as a function of modulation.

the main mirror is perfectly phased (no errors) and that because of the wind, it starts to slowly dephase. After about 5 seconds, it reaches a stationary regime.

This plot allows us to say that:

- Without AO correction, atmospheric turbulence dominates the errors in these simulations.

- The AO correction is stable in time, even if the M1 error increases.

- Without turbulence, a high (more than 95%) Strehl is achieved.

5. EXPLORATION OF THE PYRAMID WFS

5.1. Rationale

Simulations of a SCAO system using a pyramid WFS for the EELT have been made. The objective was to optimize parameters such as the SVD truncation threshold, loop gain and modulation amplitude for 3 wavefront sensing bands (R, J and K). The atmospheric model adopted has a Fried parameter r_0 of 0.13m (at 0.5 microns) and an outer scale of 25m. The number of the DM active actuators is 5402. The telescope includes a central obstruction of 28% (no spiders). The strehl is always measured in the K band. The NGS is on-axis and provides an infinitely high flux. Diffraction between the pyramids sub-pupils is taken into account.

5.2. Results

Figure 8(b) shows the Strehl as a function of loop gain and SVD threshold of 4000 modes. Red (top at 0 modulation), yellow (middle) and blue (bottom) denote K, J and R wavefront sensing bands, respectively. Natural modulation (zero amplitude) seems to show a poorer performance in all bands, and to require larger loop gains in general and as the sensing wavelength becomes bluer. Optimal loop gains are also smaller for non-zero modulations.

Figure 8(a) shows the optimal Strehl ratios obtained as a function of loop gain, for different modulation amplitudes. Notice that for larger amplitude modulations the Strehl ratio converges to a maximum value around 0.80-0.83 (in the R band this value is not reached for the parameter space investigated).

We can see that modulation is necessary on the EELT, especially at short wavelengths. This was expected, due to the saturation of the pyramid WFS measurements. Note that here we have not used Sensitivity Compensation,[16] which is known to significantly help the performance of the pyramid in a saturated regime.

6. CONCLUSIONS

In this paper, we have simulated the AO systems planned for the EELT and optimized a number of the design parameters. For the LGS AO systems, we have found that central projection of the laser is perferable to side projection, the CORR or MF algorithms are superior to a traditional COG approach, the optimum sampling is approximately 1.5 pixels per FWHM of the non-elongated spot, and that 10×10 pixels is sufficient if the laser is centrally projected. We have seen that quasi-static aberrations with a QC will be significantly worse than for a multi-pixel detector. The required number of photons from the LGS per subaperture per frame is of the order of 1000; this is to achieve a Strehl of 0.7 in K band. We have also studied correcting segmentation errors with a Shack-Hartmann WFS, finding that atmospheric turbulence dominates these errors. The pyramid WFS was also simulated for the EELT, with a conclusion that modulation of the pyramid will be necessary.

REFERENCES

1. J. Nelson, G. H. Sanders, "TMT status report,"in *Ground-based and Airborne Telescopes*, L. M. Stepp Ed., Proc. SPIE **6267**, 745-761 (2006).
2. M. W. Johns, "The Giant Magellan Telescope (GMT)," in *Ground-based and Airborne Telescopes*, L. M. Stepp Ed., Proc. SPIE **6267**, 762-776 (2006)
3. I. Hook, G. Dalton, R. Gilmozzi "Scientific requirements for a European ELT ," in *Ground-based and Airborne Telescopes*, L. M. Stepp Ed., Proc. SPIE **6267**, 726-734 (2006).
4. N. Hubin, B. L. Ellerbroek, M. Le Louarn, J.-P. Veran, E. Marchetti, G. Herriot, C. Verinaud, R. M. Clare, M. Kasper, J. Stoesz, S. Oberti, and R. Arsenault, "Adaptive Optics for Extremely Large Telescopes," Proc. IAU 60-85 (2005).
5. M. A. van Dam, A. H. Bouchez, D. Le Mignant and P. L. Wizinowich "Quasi-static aberrations induced by laser guide stars in adaptive optics," Opt. Express **14**, 7535-7540 (2006).
6. R. M. Clare, M. A. van Dam, A. H. Bouchez, "Modeling low order aberrations in laser guide star adaptive optics systems," Optics Express **15**, 4711-4725 (2007).
7. S. Thomas, T. Fusco, A. Tokovinin, M. Nicolle, V. Michau and G. Rousset, "Comparison of centroid computation algorithms in a Shack-Hartmann sensor," MNRAS 323-336 (2006).
8. M. A. van Dam, A. H. Bouchez, D. Le Mignant, R. D. Campbell, J. C. Y. Chin, S. K. Hartman, E. M. Johansson, R. Lafon, P. J. Stomski, Jr., D. M. Summers and P. L. Wizinowich, "The W. M. Keck Observatory laser guide star adaptive optics system: performance characterization," PASP **118**, 310-318 (2006).
9. L. A. Poyneer, "Scene-based Shack-Hartmann wave-front sensing: analysis and simulation," Appl. Opt. **42**, 5807-5815 (2003).
10. L. Gilles and B. Ellerbroek, "Shack-Hartmann wavefront sensing with elongated sodium laser beacons: centroiding versus matched filtering," Appl. Opt. **45**, 6568-6576 (2006).
11. S. Thomas, S. Adkins, D. Gavel, B. Ellerbroek, L. Gilles, and T. Fusco, "Study of the parameters for a polar coordinate CCD using laser guide stars," Proceedings of Adaptive Optics: Analysis and Methods (2007).
12. M. Tallon, "Contributions a l'imagerie a haute resolution angulaire: analyse de surface d'onde, source laser de reference, optique adaptative," PhD thesis, University of Nice (1989).
13. P. S. Argall, O. N. Vassiliev, R. J. Sica and M. M. Mwangi, "LIDAR measurements taken with a large-aperture liquid mirror. 2. Sodium resonance-fluorescence system," Appl. Opt. **39**, 2393-2400 (2000).
14. O. Lardiere, R. Conan, C. Bradley, K. Jackson, and G. Herriot, "A laser guide star wavefront sensor bench demonstrator for TMT," Optics Express **16**, 5527-5543 (2008).
15. N. Yaitskova and Ch. Verinaud, "Adaptive optics correction of the wavefront distortions induced by segments misalignment in Extremely Large Telescope", Ground-based and Airborne Telescopes. Edited by Stepp, Larry M.. Proceedings of the SPIE, **6267**, (2006).
16. V. Korkiakoski, C. Vrinaud, and M. Le Louarn, "Improving the performance of a pyramid wavefront sensor with modal sensitivity compensation," Appl. Opt. **47**, 79-87 (2008)